





## Gate switchable spin-orbit splitting in a MoTe<sub>2</sub>/WTe<sub>2</sub> heterostructure from first-principles calculations

Jiafeng Xie , Feihong Xu , Tianwu Wang ,\* Zhou Li,<sup>†</sup> and Guangyou Fang

*GBA Branch of Aerospace Information Research Institute, Chinese Academy of Sciences, Guangzhou 510700, China and Guangdong Provincial Key Laboratory of Terahertz Quantum Electromagnetics, Guangzhou 510700, China*

Huafeng Dong  and Xiaobin Guo

*School of Physics and Optoelectric Engineering, Guangdong University of Technology, Guangzhou 510006, China*

 (Received 21 January 2023; revised 24 March 2023; accepted 27 March 2023; published 3 April 2023)

Transition-metal dichalcogenides are good candidates for spintronic technologies owing to their giant intrinsic spin-orbit splitting. Manipulation of energy splitting is highly desirable for further practical devices. In this work, we provide a simple route to modulate spin-orbit splitting in van der Waals MoTe<sub>2</sub>/WTe<sub>2</sub> heterostructure. By introducing an external electric field pointing from MoTe<sub>2</sub> to WTe<sub>2</sub>, the spin-orbit splitting of individual layers can be switched more than 10 meV. The spin-orbit splitting of MoTe<sub>2</sub> switches from 213 meV to 204 ~ 180 meV under electric field of 0.02 ~ 0.24 V/Å. The energy splitting of WTe<sub>2</sub> switches to 490 ~ 513 meV. The underlying physics stems from interlayer charge redistribution and band repulsion, where the parallel spin in the sub-bands plays a role. Our findings provide a clue to actively control the spin-orbit splitting in transition-metal dichalcogenides, which is of great importance for developing innovative nonmagnetic spintronic devices.

DOI: [10.1103/PhysRevB.107.165101](https://doi.org/10.1103/PhysRevB.107.165101)

### I. INTRODUCTION

Spin-orbit coupling (SOC) is the interaction between spin and orbital momentum of electrons [1]. It induces energy splitting to degenerate states with different spin textures, named as spin-orbit splitting (SOS). According to the origin mechanism, the SOS can be divided into two types. One is Zeeman splitting based on spin polarization [2]. The other is Rashba and Dresselhaus split related to electric polarization, which results from the interface and crystal inversion asymmetry, respectively [3]. The magnitude of SOS represents the coupling strength and reflects the intrinsic spin properties of materials, which plays a crucial role in designing spintronic devices [4]. For example, hexagonal monolayer transition-metal dichalcogenides (TMDs, 2H-MX<sub>2</sub> with  $M = \text{Mo}, \text{W}$  and  $X = \text{S}, \text{Se}, \text{Te}$ ) with P-6m2/mmc symmetry [as shown in Fig. 1(a)] are good candidates for spintronic technologies. Because those monolayers exhibit an intrinsic SOS of several hundred meV at the valence band maximum [5–7]. The giant SOS defines two different excitons attached to the two spin-split valence sub-bands [as shown in Fig. 1(c)], which can be obviously observed by photoluminescence [8,9]. Further modulating the excitons or the intrinsic SOSs is essential for practical spintronic devices based on TMDs, including spin field-effect transistors. By introducing an external magnetic field, strong Zeeman splitting at K valley of 0.21 meV/Tesla is observed in 2H-WSe<sub>2</sub> [10], and similar results are reported in TMDs with magnetic substrates, such as EuO, CrI<sub>3</sub>, and

RbMnCl<sub>3</sub> [11–16]. Other manipulations are also effective, such as electron/hole doping [17], biaxial strain [18], and laser irradiation [19]. However, the external electric field ( $E_{\text{ext}}$ ) has little effect on valley splitting except for strong Rashba splitting near  $\Gamma$  point [20].

Different from monolayers, heterostructures are more sensitive to  $E_{\text{ext}}$ . For instance, the band gaps of TMDs-based van der Waals (vdW) heterostructures can be effectively modulated by  $E_{\text{ext}}$  [21–25], including the band alignment transition and semiconductor-semimetal transition. However, investigating the SOS modulation based on  $E_{\text{ext}}$  are still lacking due to the inversion symmetry in valence sub-bands. Inspired by the interaction between pseudospin and magnetic substrates, the pseudospin feature in monolayer TMDs may also play a role in the SOS regulation of TMD heterostructures. Among the monolayer TMDs, 2H-WTe<sub>2</sub> exhibits the largest SOS of 480 meV. It is a good candidate as substrate to interact with pseudospin in TMDs. Considering that the lattice constant of 2H-WTe<sub>2</sub> is quite different from those of other 2H-MX<sub>2</sub> (summarized in Supplemental Material, Table S1 [26]), we finally choose 2H-MoTe<sub>2</sub> as the other monolayer to on top of 2H-WTe<sub>2</sub>. Thus, we obtained the MoTe<sub>2</sub>/WTe<sub>2</sub> vdW heterostructure with small lattice mismatch (<0.2%, more details in Supplemental Material, Table S2 [26]). Zheng and coauthors [27] reported that the SOS of MoTe<sub>2</sub>/WTe<sub>2</sub> can be effectively modulated 438 ~ 78 meV by  $E_{\text{ext}}$  with 4% in-plane strain. This means that the spin splitting can be adjusted by  $E_{\text{ext}}$  when the heterostructure is stressed. However, the SOS modulation in Zheng's work is a combination result of  $E_{\text{ext}}$  and strains. For pure strain modulation, Amin and coauthors predicted that SOS of monolayer 2H-WTe<sub>2</sub> can be modulated ~20 meV at 2% (both compression and tension) strain

\* wangtw@aircas.ac.cn

<sup>†</sup> liz@aircas.ac.cn

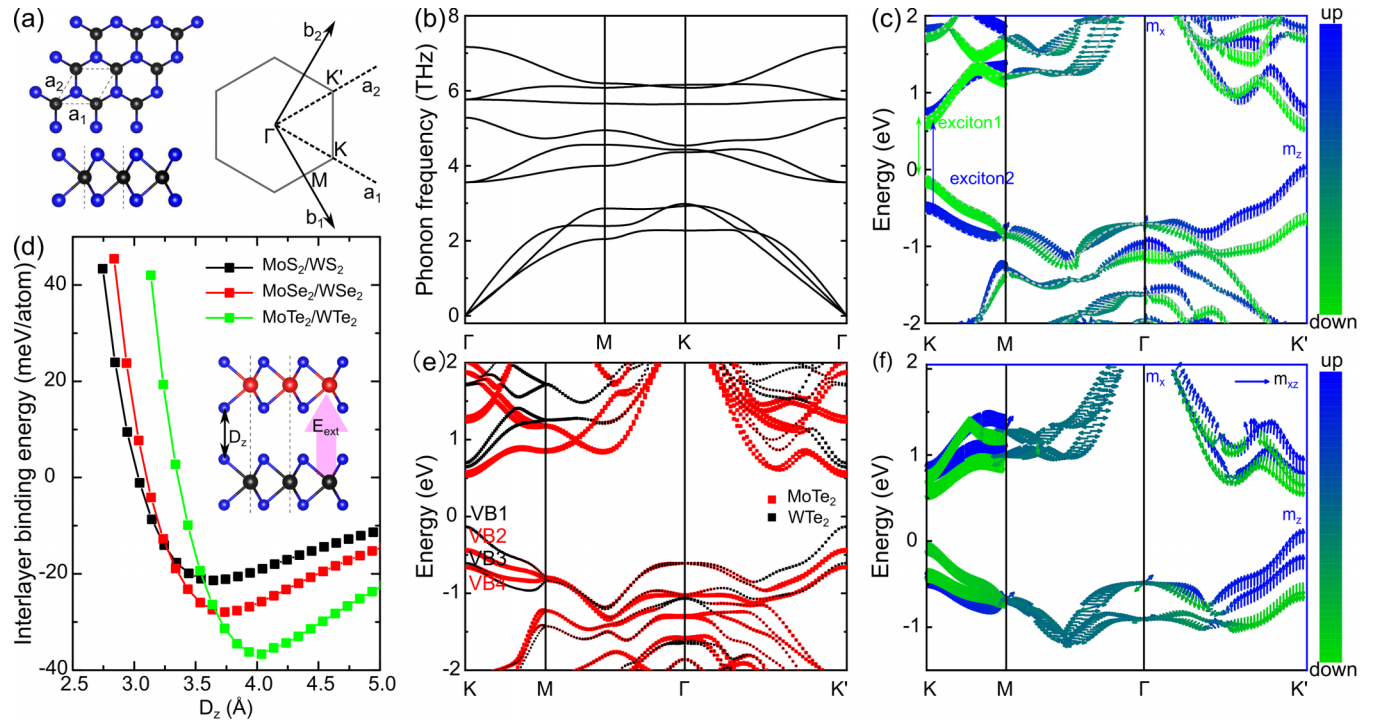


FIG. 1. Atomic and band structures of hexagonal WTe<sub>2</sub> and MoTe<sub>2</sub>/WTe<sub>2</sub> heterostructure. (a) Atomic structure and Brillouin zone of monolayer 2H-MX<sub>2</sub>. The black and blue balls denote M and X atoms, respectively. The  $a_{1/2}$  and  $b_{1/2}$  is the lattice and reciprocal vector. And  $\Gamma$ /K/M is the high-symmetry point. (b) Phonon dispersion of 2H-WTe<sub>2</sub>. (c) Band structure of 2H-WTe<sub>2</sub> with spin  $m_{xz}$  marked. The arrow lines denote the direction of pseudospin. (d) Binding energy as a function of interlayer distance  $D_z$  between AA stacking MoX<sub>2</sub>/WX<sub>2</sub>. The red, black, and blue balls denote Mo, W, and S/Se/Te atoms, respectively. (e) Band structure of MoTe<sub>2</sub>/WTe<sub>2</sub> heterostructure with spin-orbit interaction. The red and black block denote the band contribution of MoTe<sub>2</sub> and WTe<sub>2</sub>, respectively. (f) Spin-marked band structure of MoTe<sub>2</sub>/WTe<sub>2</sub> heterostructure.

[28]. Ernandes and coauthors reported that SOS of monolayer 2H-WS<sub>2</sub> can be tuned 15 meV per 1% by in-plane strain [29]. Thus, the intrinsic strain (2.3%) in their model is non-negligible for investigating SOS. The influence of  $E_{\text{ext}}$  on SOS without strain is of great importance but has not yet been fully investigated. To obtain a clearer physical picture of SOS modulation under  $E_{\text{ext}}$ , the evolution of SOS in strain-free MoTe<sub>2</sub>/WTe<sub>2</sub> is of great importance. Although the electric field along  $z$  direction has little effect on the SOS of  $d_{x^2-y^2}$  or  $d_{xy}$  orbitals, a considerable interaction between pseudospin and magnetic momentum at K/K' valley is possible to be observed when bands shift close to each other. Xie [30] and coauthors predicted that valley splitting of WSe<sub>2</sub>/CrI<sub>3</sub> can reach  $\sim 10$  meV when the bands of W: $d_{x^2-y^2} + d_{xy}$  and Cr: $d_{z^2}$  are shifted close by  $E_{\text{ext}}$ . Since the band interaction between similar orbitals (Mo: $d_{x^2-y^2} + d_{xy}$  and W: $d_{x^2-y^2} + d_{xy}$ , details are shown in Supplemental Material, Fig. S5 [26]) is stronger, larger energy splitting may be observed in K/K' valley of MoTe<sub>2</sub>/WTe<sub>2</sub>. Tunable SOSs are expected in both 2H-MoTe<sub>2</sub> and 2H-WTe<sub>2</sub> owing to their interaction of sub-bands. In addition, the nonmagnetic composition in MoTe<sub>2</sub>/WTe<sub>2</sub> provides an opportunity to tune the SOS without relying on any specific magnetic substrate

Monolayer MX<sub>2</sub> has several atomic configurations. In addition to the 2H phase, the monoclinic 1T' phase with P2<sub>1</sub>/m symmetry is also a stable polytype for WTe<sub>2</sub> and MoTe<sub>2</sub>. For 2H-WTe<sub>2</sub>, the formation energy ( $E_{\text{form}} = (E_{\text{mono}} - \sum E_{\text{atom}})/N_{\text{atom}}$ ) is  $-3.27$  eV/atom, which is slightly smaller

than that of 1T'-WTe<sub>2</sub> ( $-3.30$  eV/atom) [31]. The phonon dispersion of 2H-WTe<sub>2</sub> is depicted in Fig. 1(b). No imaginary frequency is observed, which indicates that 2H-WTe<sub>2</sub> is thermally stable. The formation energy of 2H-MoTe<sub>2</sub> ( $-3.14$  eV/atom) is also comparable to that of 1T'-MoTe<sub>2</sub> ( $-3.12$  eV/atom) [31,32] (phonon dispersion comparison is shown in the Supplemental Material, Fig. S1 [26]). It means that both 2H-MoTe<sub>2</sub> and 2H-WTe<sub>2</sub> are thermally stable. Recently, 2H-WTe<sub>2</sub> was also synthesized successfully [33,34]. In the following discussion, we use MoTe<sub>2</sub> (WTe<sub>2</sub>) to denote the 2H-MoTe<sub>2</sub> (2H-WTe<sub>2</sub>) without any specification.

In this work, we performed first-principles calculations on the electronic properties of vdW heterostructure MoTe<sub>2</sub>/WTe<sub>2</sub>. The heterostructure forms a type-II band alignment with a direct band gap of 0.67 eV at K point. The band gap can be tuned linearly to THz (106 meV) under  $E_{\text{ext}} = 0.47$  V/Å pointing from WTe<sub>2</sub> to MoTe<sub>2</sub>. The SOSs remain unchanged at  $\sim 480$  meV and  $\sim 213$  meV for WTe<sub>2</sub> and MoTe<sub>2</sub>, respectively. However, once  $E_{\text{ext}}$  switches to the opposite direction (denoting as negative), both the band gap and SOS vary in different manners. The band gap first increases to 0.76 eV at  $-0.09$  V/Å, then retains constant until  $-0.24$  V/Å, and finally linearly decreases as  $E_{\text{ext}}$  increases. Different from the band gap evolution under negative electric field, the SOSs of WTe<sub>2</sub> and MoTe<sub>2</sub> switch to 490  $\sim$  513 meV and 204  $\sim$  180 meV when  $E_{\text{ext}}$  varies from  $-0.02$  V/Å to  $-0.24$  V/Å. However, the SOSs return to their intrinsic values when  $E_{\text{ext}}$  further increases. It means that the SOSs of WTe<sub>2</sub>

and MoTe<sub>2</sub> switch over 10 meV under external electric field, which is promising for modulating the SOS with simple experimental conditions. Our findings offer a new clue to control the SOS in nonmagnetic TMDs and provide feasible reference for innovative spintronic devices.

## II. COMPUTATIONAL DETAILS

First-principles plane-wave calculations within density functional theory (DFT) using projector-augmented wave (PAW) potentials [35] were performed using the Vienna *ab initio* simulation package (VASP) [36]. The Perdew-Burke-Ernzerhof (PBE) exchange-correlation function under generalized gradient approximation (GGA) was applied in the calculations [37]. The semiempirical dispersion-corrected DFT scheme of Grimme (DFT-D2 approximation) [38] was applied to evaluate the weak interlayer vdW interaction. A vacuum space larger than 15 Å was introduced in heterostructure to avoid the interaction between periodic boundary. The plane-wave energy cutoff was set to 500 eV to ensure the convergence of total energy. The energy convergence threshold was set to 10<sup>-7</sup> eV and 10<sup>-6</sup> eV for monolayer and heterostructure, respectively. The reciprocal space was sampled by a fine grid of 15×15×1k points in the Brillouin zone (BZ) [39]. The structural relaxations were performed until the force on each individual atom is less than 0.01 eV/Å. All of our calculations have included the spin-orbit coupling (noncollinear magnetism) interaction.

## III. RESULTS AND ANALYSIS

With full relaxation of the atomic structure, the optimized lattice constants of MoTe<sub>2</sub> and WTe<sub>2</sub> are 3.549 Å and 3.551 Å, which agrees well with previous works [28,40]. It is larger than those of MoS<sub>2</sub> (3.182 Å) and MoSe<sub>2</sub> (3.317 Å) [41] owing to the larger atomic radius of Te. To be more comparable between monolayers and vdW heterostructures, we calculated the atomic structures of monolayers with DFT-D2 method. The lattice constant of WTe<sub>2</sub> (3.555 Å) is slightly larger than that obtained from PBE method, while the lattice constant of MoTe<sub>2</sub> (3.526 Å) is smaller. However, the difference of lattice constants between WTe<sub>2</sub> and MoTe<sub>2</sub> is smaller than 0.03 Å. It means the MoTe<sub>2</sub>/WTe<sub>2</sub> heterostructure may be free from strain induced by lattice mismatch. For the electronic band gap, it shows no difference between values obtained from different methods (see Supplemental Material, Fig. S2 [26]). Thus, in the following calculation, all the results are obtained with DFT-D2 method.

By stacking monolayer MoTe<sub>2</sub> directly on top of monolayer WTe<sub>2</sub>, we obtained an AA-stacking vdW heterostructure, as shown in Fig. 1(d) (inset). The atomic parameter of MoTe<sub>2</sub>/WTe<sub>2</sub> heterostructure is 3.539 Å, in good agreement with monolayers, resulting in lattice mismatch less than 0.2%. In order to evaluate the thermal stability of the heterostructure, we calculated the binding (formation) energy [42,43],

$$E_{\text{binding}} = \frac{(E_H - E_{\text{MoTe}_2} - E_{\text{WTe}_2})}{N_{\text{atom}}}. \quad (1)$$

where  $E_\alpha$  represents the total energy of  $\alpha$  (heterostructure, MoTe<sub>2</sub>, and WTe<sub>2</sub>, respectively), and  $N_{\text{atom}}$  represents the total number of atoms in the unit cell. As depicted in Fig. 1(d),

the binding energy of MoTe<sub>2</sub>/WTe<sub>2</sub> is -36.65 meV/atom, and the corresponding interlayer distance ( $D_z$ ) is 4.04 Å. For MoS<sub>2</sub>/WS<sub>2</sub>, however, the binding energy is smaller (-21.34 meV/atom with  $D_z = 3.64$  Å), resulting from the smaller repulsion between the AA-stacked S atoms. These binding energies agree well with those of other vdW heterostructures and are comparable to those of bilayers [44,45], indicating that the MoTe<sub>2</sub>/WTe<sub>2</sub> heterostructure is thermally stable.

Figure 1(e) depicts the electronic structure of MoTe<sub>2</sub>/WTe<sub>2</sub>, and a direct band gap of 0.67 eV is observed. It shows a type-II band alignment at K/K' point, where the WTe<sub>2</sub> contributes to the valence band maximum (VBM) and the MoTe<sub>2</sub> contributes to the conduction band minimum (CBM). Our results are consistent with Ref. [27], except for a slight difference at the extreme valley near the Fermi energy level. Type-II heterostructures always possess separated electrons and holes in excited states. Thus, the excited electrons in MoTe<sub>2</sub> will couple with the holes in WTe<sub>2</sub> and form interlayer excitons. Owing to the intrinsic SOC in Mo and W, large energy splitting occurs in the VBM at K valley, 480 meV and 213 meV for WTe<sub>2</sub> and MoTe<sub>2</sub>, respectively. Additionally, there are four valence bands (VB $i$ ,  $i = 1, 2, 3, 4$ ) near K, as depicted in Fig. 1(e). The VB1 (VB3) and VB2 (VB4) are contributed by different layers, however, their pseudospin features at K point are parallel along  $z$  direction—as shown in Fig. 1(f). In addition, the parallel pseudospin becomes antiparallel and energy degenerate near  $\Gamma$  point. Thus, it is convenient for the external electric field to induce Rashba splitting in Ref. [20]. As the photoluminescence quantum yield is proportional to the transition dipole moment (TDM),  $P_{a \rightarrow b} = \langle \varphi_a | \mathbf{r} | \varphi_b \rangle$ , where  $\varphi_{a/b}$  is the initial/final state, and  $\mathbf{r}$  is the electric dipole operator. The TDM determines how the system will interact with an electromagnetic wave, and the square of the magnitude ( $P^2$ ) gives the strength of the interaction. In Supplemental Material, Fig. S3 [26], we calculated  $P^2$  between VB1 and CBM by using VASPKIT [46]. The  $P^2$  as a function of reciprocal vector, and shows high transition probabilities between VB1 and CBM at K/K'. In other words, MoTe<sub>2</sub>/WTe<sub>2</sub> is a good candidate for infrared radiation based on interlayer excitons.

Owing to the different electronegativities of chemical compounds, an effective electric dipole exists at the interface. It allows effective electrical control of the band gap, as shown in Fig. 2(a), which may be impossible in individual layers (in Supplemental Material, Fig. S4 [26]). By introducing an external electric field ( $E_{\text{ext}}$ ) pointing from WTe<sub>2</sub> to MoTe<sub>2</sub> [as defined in Fig. 1(d)], the conduction bands of MoTe<sub>2</sub> (red blocks) shift close to the Fermi level, resulting in a band gap decrease, as depicted in the region I of Fig. 2(b). As  $E_{\text{ext}}$  increases to 0.47 V/Å, the band gap decreases linearly to 106 meV, indicating a giant Stark effect. The decrement of the band gap is  $\sim 22$  meV per 0.01 V/Å, and no transition of band alignment is observed.

When  $E_{\text{ext}}$  switches to the opposite direction (denoting as negative), the evolution of the band gap shows a quite distinct manner. The negative  $E_{\text{ext}}$  induces conduction bands of MoTe<sub>2</sub> to rise up and be away from the Fermi energy, resulting in an increase of band gap, as depicted in region II of Fig. 2(a). The band gap reaches its maximum of 0.76 eV at electric field of

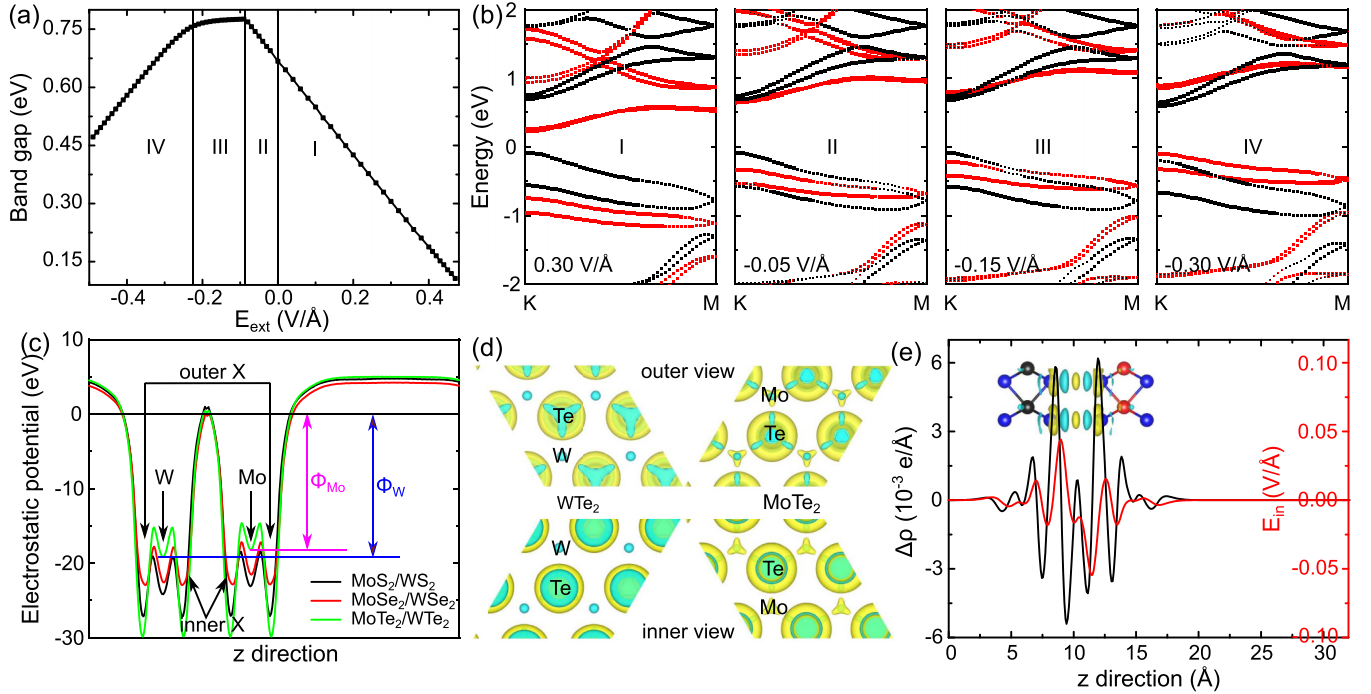


FIG. 2. Electronic properties of MoTe<sub>2</sub>/WTe<sub>2</sub> under external electric field. (a) Evolution of band gap of MoTe<sub>2</sub>/WTe<sub>2</sub> as a function of external electric field ( $E_{\text{ext}}$ ). The positive direction is denoted in Fig. 1(d). (b) Band structure of MoTe<sub>2</sub>/WTe<sub>2</sub> under different  $E_{\text{ext}}$ . (c) Electrostatic potential of MoX<sub>2</sub>/WX<sub>2</sub>. (d) Inner and outer view of charge density difference. The yellow and cyan isosurfaces denote positive and negative values, respectively. (Isosurface is  $8.5 \times 10^{-5} e/\text{Å}^3$ .) (e) Charge density difference ( $\Delta\rho$ , black line) and internal electric field ( $E_{\text{in}}$ , red line) of MoTe<sub>2</sub>/WTe<sub>2</sub> along  $z$  direction. The inset is the side view of charge difference. (Isosurface is  $8.5 \times 10^{-5} e/\text{Å}^3$ .)

$-0.09 \text{ V/Å}$ . The reduced band gap under enlarging  $E_{\text{ext}}$  in region II is also observed in MoS<sub>2</sub>/WS<sub>2</sub> and MoSe<sub>2</sub>/WSe<sub>2</sub> heterostructures [45,47]. It owes to the effect of spontaneous electric polarization, which is introduced by the electronegativity difference between the W and Mo atoms.

To obtain a clearer understanding of the underlying physics of the asymmetric regulation of electric field where electronegativity plays a role, we calculated the electrostatic potential of MoTe<sub>2</sub>/WTe<sub>2</sub> along  $z$  direction. Based on the one-dimensional (1D)-Poisson equation  $\partial^2\Phi/\partial z^2 = -\rho(z)/\epsilon_0$ , the electric potential  $\Delta\Phi$  can be obtained from the charge density  $\rho$ , which can be directly obtained from first-principles calculations. As shown in Fig. 2(c), a large and wide barrier appears in the interlayer region of MoTe<sub>2</sub>/WTe<sub>2</sub> heterostructure due to the large interlayer distance and vdW interaction. A deep valley appears at the spatial location of the ions. Owing to the larger electronegativity, the electrostatic potential of W ( $\Phi_W$ ) is slightly lower than that of Mo ( $\Phi_{Mo}$ ). It introduces charge redistribution and a built-in electric field (pointing from W to Mo) near the interface. To clarify the charge redistribution and internal electric field, we calculated the differential charge density  $\Delta\rho$  and internal electric field  $E_{\text{in}}$  of MoTe<sub>2</sub>/WTe<sub>2</sub>, which are described as,

$$\Delta\rho(x, y, z) = \rho_H(x, y, z) - \rho_{\text{MoTe}_2}(x, y, z) - \rho_{\text{WTe}_2}(x, y, z) \quad (2)$$

$$\Delta\rho(z) = \int \rho_H(x, y, z) dx dy - \int \rho_{\text{MoTe}_2}(x, y, z) dx dy - \int \rho_{\text{WTe}_2}(x, y, z) dx dy \quad (3)$$

$$E_{\text{in}}(z) = \frac{1}{2S\epsilon_0} \left( \int_{-\infty}^z \Delta\rho(z') dz' - \int_z^{\infty} \Delta\rho(z') dz' \right) \quad (4)$$

where  $\rho_\alpha$  stands for the charge density of  $\alpha$  (heterostructure, MoTe<sub>2</sub>, and WTe<sub>2</sub>, respectively),  $S$  is the area of unit cell, and  $\epsilon_0$  is the permittivity of vacuum.

The inner and outer views of  $\Delta\rho(x, y, z)$  are depicted in Fig. 2(d), and the yellow and cyan isosurfaces correspond to positive (charge accumulation) and negative values (charge depletion), respectively. For WTe<sub>2</sub>, the charge densities of W (cyan circles) and the outer Te (cyan triangle) atoms are depleted, while that of the inner Te (yellow circles) atoms are accumulated. In addition, cyan circles are observed near the inner Te atoms in the interlayer region. This means that the main redistribution of charge occurs around the inner Te atoms and the adjacent W-Te bonds. For MoTe<sub>2</sub>, similarly, charge redistribution near the interlayer region is also observed. The integral charge density  $\Delta\rho(z)$  is depicted in Fig. 2(e) (black line). In addition to charge redistribution in individual layer, charge accumulation is also observed in the interlayer region owing to the vdW interaction. The internal electric field  $E_{\text{in}}$  is zero at locations far away from individual layer owing to the electrostatic balance, such as the  $z < 2.5 \text{ Å}$  and  $z > 18 \text{ Å}$  in Fig. 2(e) (red line). However, when two layers come close and interact with each other, the  $E_{\text{in}}$  in the interlayer region varies from positive to negative, corresponding to charge depletion in WTe<sub>2</sub>. Thus, charge transfer occurs from WTe<sub>2</sub> to MoTe<sub>2</sub>, and an intrinsic electric field is induced, pointing from WTe<sub>2</sub> to MoTe<sub>2</sub>. In addition, this built-in electric field in  $10^{-2} \text{ V/Å}$  magnitude will serve as a driving force to effectively improve

the band gap modulation under positive  $E_{\text{ext}}$ , as discussed above. It will pull photogenerated electrons from  $\text{MoTe}_2$  to  $\text{WTe}_2$  and holes from  $\text{WTe}_2$  to  $\text{MoTe}_2$ , increasing the inter-layer electron-hole recombination rate.

When the negative  $E_{\text{ext}}$  further increases, a band alignment transition from type II to type I is observed. As shown in region III of Fig. 2(b), both the VBM and CBM are contributed by  $\text{WTe}_2$ , meaning that the band gap is dominated by  $\text{WTe}_2$ . The band gap remains constant under  $-0.09 \text{ V}/\text{\AA} \sim -0.24 \text{ V}/\text{\AA}$ . This flat band gap evolution in region III indicates that the electric field effect on band gap of individual layers is negligible, which is in good agreement with that of a single layer (in Supplemental Material, Fig. S4 [26]). Similar band gap variation is also observed in other heterostructures whose band alignment also transforms from type II to type I under  $E_{\text{ext}}$ , such as  $\text{WSe}_2/\text{CrI}_3$  [30],  $\text{MoS}_2/\text{WS}_2$  [45], and  $\text{MoSe}_2/\text{WSe}_2$  [47]. Lastly, as shown in region IV of Fig. 2(b), the VBM of  $\text{MoTe}_2$  rises to higher energy than that of  $\text{WTe}_2$ . The  $\text{MoTe}_2/\text{WTe}_2$  returns to type-II band alignment, where  $\text{MoTe}_2$  contributes the VBM and  $\text{WTe}_2$  contributes the CBM. As a consequence, an effective band gap evolution, which is similar to that in region I, is shown in Fig. 2(a).

Although the positive  $E_{\text{ext}}$  has an obvious regulation on the electronic band gap of  $\text{MoTe}_2/\text{WTe}_2$ , it has little influence on the SOS of  $\text{MoTe}_2$  or  $\text{WTe}_2$ . As shown in region I' of Fig. 3(a), the SOS of  $\text{MoTe}_2$  in valence sub-bands decreases slightly to 214 meV under positive  $E_{\text{ext}}$ . For the electric field of  $0.10 \text{ V}/\text{\AA}$ , the bands of  $\text{MoTe}_2$  (VB2 and VB4) shift down and move away from the Fermi level, as shown in Fig. 3(d). Meanwhile, the pseudospin of VB1 (VB2) and VB3 (VB4) are mainly contributed by  $\text{WTe}_2$  ( $\text{MoTe}_2$ ), and exhibit up and down features at  $K'$ , respectively. Owing to the parallel spin (marked by blue rectangles) and small energy difference, band hybridization is observed in the  $\Gamma$ - $K'$  direction, as depicted in Figs. 3(d)–3(e). The energy difference between VB2 and VB3 is also quite small at  $K'$ , but no band interaction is observed due to the antiparallel spin (marked by green rectangle). For negative  $E_{\text{ext}}$  larger than  $-0.24 \text{ V}/\text{\AA}$ , in region III' of Fig. 3(a), the SOS also decreases slightly by several meV.

It is known that the Rashba effect is of great importance in 2D materials. We carefully checked the valence band dispersions near  $\Gamma$  under  $E_{\text{ext}}$ . Owing to the internal electric field, the vdW heterostructure  $\text{MoTe}_2/\text{WTe}_2$  exhibits intrinsic Rashba splitting with a momentum offset of  $\sim 0.07 \text{\AA}^{-1}$  and an energy splitting of  $\sim 3.5 \text{ meV}$ , as depicted in Fig. 3(b). The spin texture near  $\Gamma$  lies in the  $xy$  plane, and it shows opposite  $m_x$  along  $\Gamma$ - $K'$  and  $\Gamma$ - $M$  directions, as shown in Fig. 3(c). Similar Rashba splitting was also observed in monolayers under  $E_{\text{ext}}$ , such as  $\text{MoSe}_2$ ,  $\text{MoS}_2$ , and  $\text{WS}_2$  [20]. The intrinsic Rashba splitting seems unchanged under electric field of  $0.10 \text{ V}/\text{\AA}$ . Whereas, the Rashba energy decreases to  $\sim 2.2 \text{ meV}$  when  $E_{\text{ext}}$  is  $-0.10 \text{ V}/\text{\AA}$ . And when  $E_{\text{ext}} = 0.47 \text{ V}/\text{\AA}$  is applied, the spin momentum near  $\Gamma$  is largely suppressed, resulting in a smaller momentum offset ( $\sim 0.02 \text{\AA}^{-1}$ ) and energy splitting ( $\sim 0.5 \text{ meV}$ ). Thus, the variation of SOS with several meV under  $E_{\text{ext}}$  can be attributed to Rashba effect.

However, the SOS of  $\text{MoTe}_2$  drops to 193 meV under electric field of  $-0.03 \text{ V}/\text{\AA}$ , and then varies from 180 meV ( $-0.24 \text{ V}/\text{\AA}$ ) to 204 meV ( $-0.10 \text{ V}/\text{\AA}$ ) in the region II' of

Fig. 3(a). As shown in Fig. 3(d), II', VB4 rises to a higher energy than VB3, and the sub-bands of  $\text{MoTe}_2$  are intercalated in those of  $\text{WTe}_2$ . The VB1 (VB3) and VB2 (VB4) show band repulsion of each other because of their aligned spin, resulting in larger SOS in  $\text{WTe}_2$  and smaller SOS in  $\text{MoTe}_2$ . This means that the SOS can be modulated more than 10 meV ( $\sim 5\%$ ) by negative  $E_{\text{ext}}$  (pointing from  $\text{MoTe}_2$  to  $\text{WTe}_2$ ). Such a large SOS is comparable to Zeeman splitting of TMD monolayers under an external magnetic field of  $\sim 5$  Tesla. More excitingly, a similar switchable transition of SOS is also observed in  $\text{WTe}_2$ , the SOS of 480 meV switches to 489 meV ( $-0.10 \text{ V}/\text{\AA}$ )  $\sim 513 \text{ meV}$  ( $-0.24 \text{ V}/\text{\AA}$ ). Thus, the SOS of individual monolayers in heterostructure can be effectively switched by an external electric field without strain or magnetic field (substrate). In other words, this intrinsic SOS feature can be further tuned by external gate volts, which is promising for spintronic photoelectronic devices.

To explore the underlying physics of the gate switchable SOS, we carefully checked the band dispersions and corresponding spin texture of  $\text{VB}_i$  at the critical situation  $E_{\text{ext}} = -0.02 \text{ V}/\text{\AA}$ , as shown at the bottom of Figs. 3(d)–3(e). Due to the parallel valley pseudospin and the same  $d_{xy} + d_{x^2-y^2}$  orbitals, obvious band hybridization is observed between VB3 and VB4 at  $K'$ . Charge redistribution is also observed in the partial (band decomposed) charge density, as depicted in Fig. 3(f). For VB1, the charge density is located on W atoms, which is in agreement with  $\text{W}:d_{xy} + d_{x^2-y^2}$  dominated band of VB1 at  $K'$ . In contrast, the charge density of VB2 is individually distributed on Mo atoms. However, the spatial charge distribution of VB3 resides on W atoms as well as Mo atoms. This is also true for VB4 except for little difference that charge density are more diffusion on Mo atoms. This induces higher eigenvalue of VB3 than that of VB4, resulting in smaller SOS of  $\text{MoTe}_2$  compared to  $E_{\text{ext}} = 0.00 \text{ V}/\text{\AA}$ . In addition, the parallel spin makes it possible for charge density to transfer to each other, as mentioned in Ref. [30]. Thus, the band interaction and charge transfer related to valley pseudospin play a key role in the gate switchable SOS in  $\text{MoTe}_2/\text{WTe}_2$  heterostructure. In other words, a clear physical image comes to our eyes that  $E_{\text{ext}}$  induces bands with parallel pseudospin close to each other, introducing charge transfer and charge redistribution in sub-bands  $\text{VB}_i$  at  $K/K'$ , which leads to gate switchable SOSs.

The realism of the gate modulated SOS in  $\text{MoTe}_2/\text{WTe}_2$  heterostructure is depicted in Fig. 4, which is similar to the analytical models proposed in  $\text{MoTe}_2/\text{EuO}$  [12] and  $\text{MoS}_2/\text{MoTe}_2$  [48]. A voltage gate is placed on the top of heterostructure to generate an electrostatic modulation along  $z$  direction, and it plays the same role as the external electric field described in our computation above. The electrostatic method shifts the Fermi level and introduces band interaction between valleys of  $\text{MoTe}_2$  and  $\text{WTe}_2$ , resulting in a gate switchable SOS in  $\text{MoTe}_2/\text{WTe}_2$  heterostructure. Considering typical TMDs samples will have edges or impurities, additional bands may present near the Fermi level. The metallic edge states with spin polarization has been predicted in zigzag  $\text{MoTe}_2$  and other TMDs [15,49,50]. It may suppress the electric field modulation of SOS in

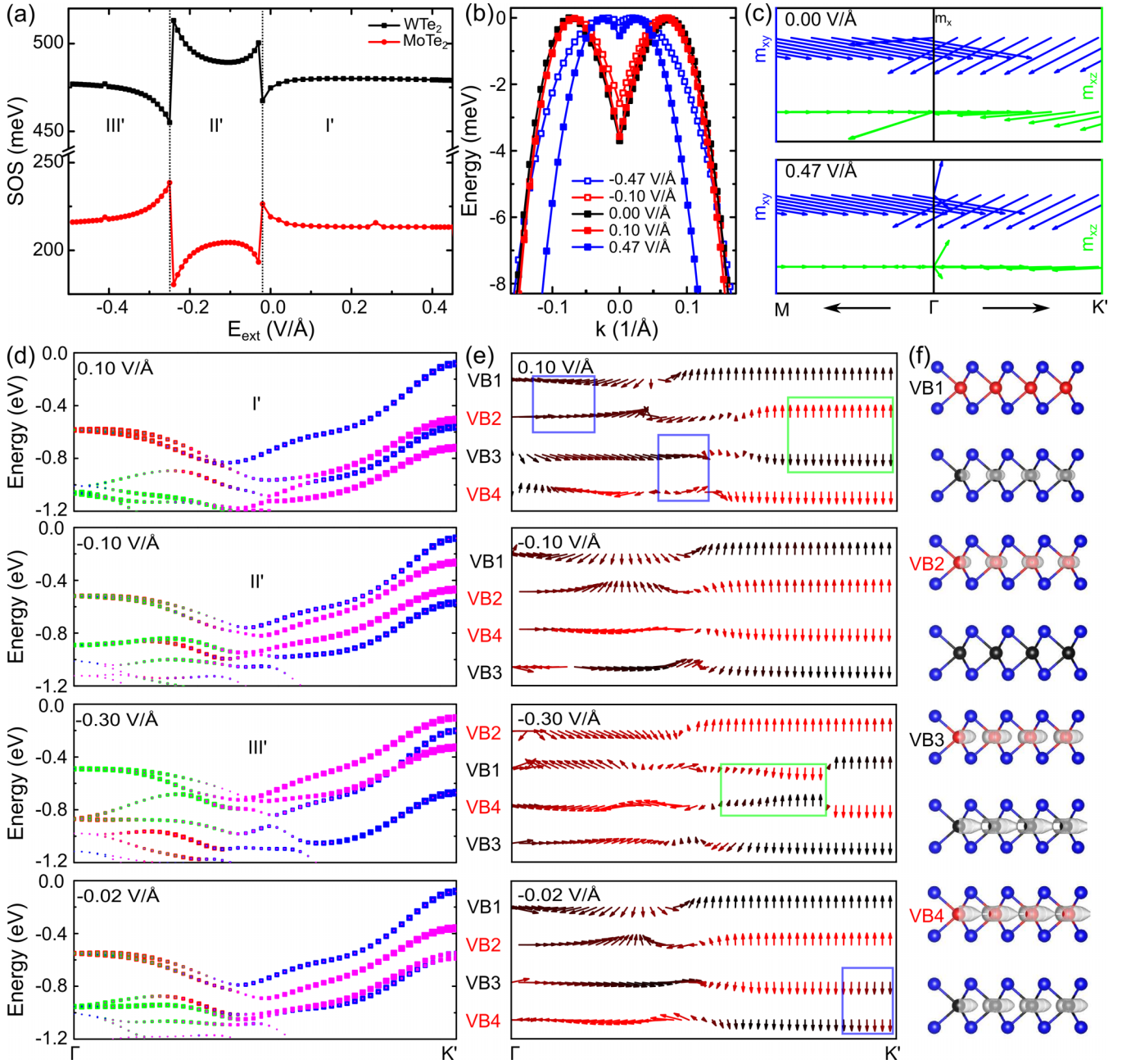


FIG. 3. Spin-orbit splitting and projected bands of MoTe<sub>2</sub>/WTe<sub>2</sub> under external electric field. (a) Spin-orbit splitting (SOS) as a function of external electric field ( $E_{\text{ext}}$ ). (b) Valence band maximum near  $\Gamma$  under  $E_{\text{ext}}$  ( $-0.47$  V/Å,  $-0.10$  V/Å,  $0.00$  V/Å,  $0.10$  V/Å, and  $0.47$  V/Å). (c) Spin texture of VBM near  $\Gamma$  under  $E_{\text{ext}}$ . Blue and green arrows denote  $m_{xy}$  and  $m_{xz}$ , respectively. (d) Orbital projected band dispersion of VB<sub>*i*</sub> under  $E_{\text{ext}}$  of  $0.10$  V/Å,  $-0.10$  V/Å,  $-0.30$  V/Å, and  $-0.02$  V/Å, respectively. The blue, pink, red, and green blocks denote contribution of W: $d_{xy} + d_{x^2-y^2}$ , Mo: $d_{xy} + d_{x^2-y^2}$ , W: $d_{z^2}$ , and Mo: $d_{z^2}$ , respectively. (e) The spin texture  $m_{xz}$  of VB<sub>*i*</sub> under  $E_{\text{ext}}$  of  $0.10$  V/Å,  $-0.10$  V/Å,  $-0.30$  V/Å, and  $-0.02$  V/Å, respectively. The black and red colors denote contribution of WTe<sub>2</sub> and MoTe<sub>2</sub>, respectively. (f) Partial charge density of VB<sub>*i*</sub> at K' under  $E_{\text{ext}}$  of  $-0.02$  V/Å. (Isosurface is  $0.02$  e/Å<sup>3</sup>).

valleys. To mitigate this, we propose applying a transverse electric field along zigzag or armchair direction to tune the edge state from metallic to semiconducting [49]. Thus, the transverse electric field would preserve the SOS against undesired metallic states. Substrate is another important factor for device performance. Traditional silicon or silicon dioxide substrate can introduce external strain to ultrathin film due

to lattice mismatch [51]. However, the SOSs of MoTe<sub>2</sub> and WTe<sub>2</sub> are quite sensitive to strain. For MoTe<sub>2</sub>/WTe<sub>2</sub> vdW heterostructures, wide gap dielectric materials with vdW interface (such as hexagonal boron nitride) are preferable substrate to preserve high performance and avoid undesired effects. In summary, by carefully choosing the substrate and applying a suitable transverse electric field, the gate switchable

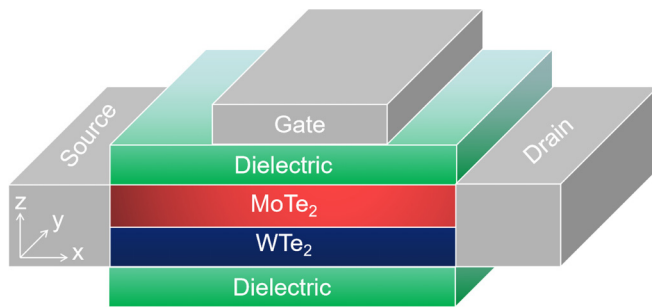


FIG. 4. Schematic of vertical electric field-modulated SOS device of MoTe<sub>2</sub>/WTe<sub>2</sub> heterostructure.

SOS in MoTe<sub>2</sub>/WTe<sub>2</sub> holds great promise for spintronic devices.

#### IV. CONCLUSION

In conclusion, the electric field-mediated spin-orbit splitting in the vdW heterostructure MoTe<sub>2</sub>/WTe<sub>2</sub> is investigated based on first-principles calculations. The results show that gate switchable spin-orbit splitting is realized under external

electric field pointing from WTe<sub>2</sub> to MoTe<sub>2</sub>. The splitting in MoTe<sub>2</sub> is 213–204 meV, and that in WTe<sub>2</sub> is 480–490 meV. The underlying physics originates from the distinct exchange interaction with the pseudospin of the valence bands related to spin-orbit coupling. The electric field shifts valence bands of MoTe<sub>2</sub> and WTe<sub>2</sub> close together with small energy difference, and parallel pseudospin introduces charge transfer and band hybridization, leading to an enhanced spin-orbit splitting. Our findings imply that the spin-orbit splitting of MoTe<sub>2</sub>/WTe<sub>2</sub> can be controlled by electric field where the band interaction between valley pseudospin plays a key role, and provide new clues to regulate spin-orbit coupling in nonmagnetic systems, which is crucial for spintronics devices.

#### ACKNOWLEDGMENTS

This work was supported by the National Natural Science Foundation of China (Grants No. 61988102, No. 12274424, and No. 11904056), Key Research and Development Program of Guangdong Province (2019B090917007), Science and Technology Planning Project of Guangdong Province (2019B090909011), Guangzhou basic and applied basic research Project (No. 202102020053).

- [1] A. Soumyanarayanan, N. Reyren, A. Fert, and C. Panagopoulos, *Nature (London)* **539**, 509 (2016).
- [2] S. Zihlmann, A. W. Cummings, J. H. Garcia, M. Kedves, K. Watanabe, T. Taniguchi, C. Schönberger, and P. Makk, *Phys. Rev. B* **97**, 075434 (2018).
- [3] A. Manchon, H. C. Koo, J. Nitta, S. M. Frolov, and R. A. Duine, *Nature Mater.* **14**, 871 (2015).
- [4] K. Premasiri and X. P. A. Gao, *J. Phys.: Condens. Matter* **31**, 193001 (2019).
- [5] D. W. Latzke, W. Zhang, A. Suslu, T.-R. Chang, H. Lin, H.-T. Jeng, S. Tongay, J. Wu, A. Bansil *et al.*, *Phys. Rev. B* **91**, 235202 (2015).
- [6] Y. Bai, *Integrated Ferroelectrics* **182**, 30 (2017).
- [7] H. G. Kim and H. J. Choi, *Phys. Rev. B* **103**, 085404 (2021).
- [8] J. Yang, T. Lu, Y. W. Myint, J. Pei, D. Macdonald, J. C. Zheng, and Y. Lu, *ACS Nano* **9**, 6603 (2015).
- [9] B. Han, C. Robert, E. Courtade, M. Manca, S. Shree, T. Amand *et al.*, *Phys. Rev. X* **8**, 031073 (2018).
- [10] W. Liu, C. Luo, X. Tang, X. Peng, and J. Zhong, *AIP Adv.* **9**, 045222 (2019).
- [11] J. Qi, X. Li, Q. Niu, and J. Feng, *Phys. Rev. B* **92**, 121403(R) (2015).
- [12] Q. Zhang, S. A. Yang, W. Mi, Y. Cheng, and U. Schwingenschlögl, *Adv. Mater.* **28**, 959 (2016).
- [13] B. Scharf, G. Xu, A. Matos-Abiague, and I. Žutić, *Phys. Rev. Lett.* **119**, 127403 (2017).
- [14] N. Li, J. Zhang, Y. Xue, T. Zhou, and Z. Yang, *Phys. Chem. Chem. Phys.* **20**, 3805 (2018).
- [15] N. Cortés, O. Ávalos-Ovando, L. Rosales, P. A. Orellana, and S. E. Ulloa, *Phys. Rev. Lett.* **122**, 086401 (2019).
- [16] T. Hu, G.-D. Zhao, H. Gao, Y. Wu, J. Hong, A. Stroppa, and W. Ren, *Phys. Rev. B* **101**, 125401 (2020).
- [17] J. Chen, K. Wu, H. Ma, W. Hu, and J. Yang, *RSC Adv.* **10**, 6388 (2020).
- [18] M. A. U. Absor, I. Santoso, Harsojo, K. Abraha, F. Ishii, and M. Saito, *J. Appl. Phys.* **122**, 153905 (2017).
- [19] X. Liang, C. Qin, Y. Gao, S. Han, G. Zhang, R. Chen, J. Hu, L. Xiao, and S. Jia, *Nanoscale* **13**, 8966 (2021).
- [20] C. Cheng, J.-T. Sun, X.-R. Chen, H.-X. Fu, and S. Meng, *Nanoscale* **8**, 17854 (2016).
- [21] W. Li, T. Wang, X. Dai, X. Wang, C. Zhai, Y. Ma, S. Chang, and Y. Tang, *Solid State Commun.* **250**, 9 (2017).
- [22] L. A. Jauregui, Y. Joe Andrew, K. Pistunova, D. S. Wild, A. A. High, Y. Zhou, G. Scuri, K. D. Greve, A. Sushko *et al.*, *Science* **366**, 870 (2019).
- [23] B. Marfoua and J. Hong, *Nanotechnology* **31**, 425702 (2020).
- [24] Y. Liu and X. Cheng, *Phys. E* **108**, 90 (2019).
- [25] I. Khan, B. Morfoua, and J. Hong, *npj 2D Mater Appl* **5**, 10 (2021).
- [26] See Supplemental Material at <http://link.aps.org/supplemental/10.1103/PhysRevB.107.165101> for additional data including the phonon dispersion of monolayer MTe<sub>2</sub>; the band structure of monolayer MTe<sub>2</sub> calculated by different methods; the band evolution of monolayer MTe<sub>2</sub>; the transition dipole moment of MoTe<sub>2</sub>/WTe<sub>2</sub>; the projected band structure of MoTe<sub>2</sub>/WTe<sub>2</sub>; and lattice constant data.
- [27] Z. Zheng, X. Wang, and W. Mi, *J. Phys.: Condens. Matter* **28**, 505003 (2016).
- [28] B. Amin, T. P. Kaloni, and U. Schwingenschlögl, *RSC Adv.* **4**, 34561 (2014).
- [29] C. Ernanandes, L. Khalil, H. Henck, M.-Q. Zhao, J. Chaste, F. Oehler, A. T. C. Johnson, M. C. Asensio, D. Pierucci, M. Pala, J. Avila, and A. Ouerghi, *Nanomaterials* **11**, 2921 (2021).
- [30] J. Xie, L. Jia, H. Shi, D. Yang, and M. Si, *Jpn. J. Appl. Phys.* **58**, 010906 (2019).

- [31] H. H. Huang, X. Fan, D. J. Singh, H. Chen, Q. Jiang, and W. T. Zheng, *Phys. Chem. Chem. Phys.* **18**, 4086 (2016).
- [32] M. Kan, H. Nam, Y. H. Lee, and Q. Sun, *Phys. Chem. Chem. Phys.* **17**, 14866 (2015).
- [33] S. Li, F.-c. Lei, X. Peng, R.-q. Wang, J.-f. Xie, Y.-p. Wu, and D.-s. Li, *Inorg. Chem.* **59**, 11935 (2020).
- [34] M. S. Sokolikova and C. Mattevi, *Chem. Soc. Rev.* **49**, 3952 (2020).
- [35] P. E. Blöchl, *Phys. Rev. B* **50**, 17953 (1994).
- [36] G. Kresse and J. Hafner, *Phys. Rev. B* **47**, 558 (1993).
- [37] J. P. Perdew, K. Burke, and M. Ernzerhof, *Phys. Rev. Lett.* **77**, 3865 (1996).
- [38] S. Grimme, *J. Comput. Chem.* **27**, 1787 (2006).
- [39] H. J. Monkhorst and J. D. Pack, *Phys. Rev. B* **13**, 5188 (1976).
- [40] J. Kang, S. Tongay, J. Zhou, J. Li, and J. Wu, *Appl. Phys. Lett.* **102**, 012111 (2013).
- [41] J. Gusakova, X. Wang, L. Y. Shiau, A. Krivosheeva, V. Shaposhnikov, V. Borisenko, V. Gusakov, and B. K. Tay, *Phys. Status Solidi A* **214**, 1700218 (2017).
- [42] J. Xie, Q. Luo, L. Jia, Z. Zhang, H. Shi, D. Yang, and M. Si, *Europhys. Lett.* **121**, 27002 (2018).
- [43] H. Zeng, R.-S. Chen, and G. Yao, *Adv. Electron. Mater.* **6**, 1901024 (2020).
- [44] P. Tao, H.-H. Guo, T. Yang, and Z.-D. Zhang, *Chin. Phys. B* **23**, 106801 (2013).
- [45] W. Li, T. Wang, X. Dai, X. Wang, C. Zhai, Y. Ma, and S. Chang, *Solid State Commun.* **225**, 32 (2016).
- [46] V. Wang, N. Xu, J. C. Liu, G. Tang, and W. T. Geng, *Comput. Phys. Commun.* **267**, 108033 (2021).
- [47] F. Zhang, W. Li, and X. Dai, *Solid State Commun.* **266**, 11 (2017).
- [48] Y. Balaji, Q. Smets, Á. Szabo, M. Mascaro, D. Lin, I. Asselberghs, L. Radu, M. Luisier, and G. Groeseneken, *Adv. Funct. Mater.* **30**, 1905970 (2020).
- [49] F. Khoeini, Kh. Shakouri, and F. M. Peeters, *Phys. Rev. B* **94**, 125412 (2016).
- [50] N. Cortés, O. Ávalos-Ovando, and S. E. Ulloa, *Phys. Rev. B* **101**, 201108(R) (2020).
- [51] Z. Dai, L. Liu, and Z. Zhang, *Adv. Mater.* **31**, 1805417 (2019).